

## Spatial configurations and temperature profiles in nonequilibrium steady state of two-species trapped ion systems

A. Ruiz-García  and D. Alonso

*Departamento de Física, Universidad de La Laguna, La Laguna 38203, Spain  
and IUEA Instituto Universitario de Estudios Avanzados, Universidad de La Laguna, La Laguna 38203, Spain*

 (Received 18 October 2019; revised manuscript received 9 December 2019; published 27 January 2020)

We study Coulomb crystals containing two ion species simultaneously confined in radio frequency traps and coupled to different thermal reservoirs located in two separate regions. We use a three-dimensional model to simulate the trapped bicrystal and show in a numerically rigorous manner the effects of the mass dependence of the trapping frequencies on the underlying nonequilibrium dynamics and the temperature profiles. By solving the classical Langevin equations of motion, we obtain the spatial probability densities of the two ion species and the kinetic temperature profiles across the axial direction of the trap in the nonequilibrium steady state. We analyze trapping conditions leading to bicrystals that exhibit ion conformations ranging from a linear chain of alternating ion species to two- and three-dimensional configurations. The results evidence the spatial segregation of the two ion species due to the mass dependence of the trapping frequencies and the increase of ion delocalization for heavier ion species and/or weaker trapping confinements. We also show the correlation between the increase of the temperature gradient in the bulk and this enhancement of ion delocalization through the trap.

DOI: [10.1103/PhysRevE.101.012129](https://doi.org/10.1103/PhysRevE.101.012129)

### I. INTRODUCTION

In recent years Coulomb crystals of ions confined in electromagnetic traps and interacting with laser beams have become a particularly convenient platform to shed some light on the intriguing issue of heat transport at the microscopic level [1–11]. Surprisingly, while the flow of heat through a medium exposed to a temperature gradient is a ubiquitous phenomenon in our daily lives, the conditions that must be satisfied at the microscopic level in a system for heat conduction to take place according to the ordinary circumstances predicted by Fourier's law are far from clear [12,13]. In fact, it has been shown that spatially constrained atomic systems, such as carbon nanotubes or molecular junctions, can exhibit an anomalous heat transport, with nonlinear temperature profiles and a divergence of the thermal conductivity with the size of the system [14–16]. Within this context Coulomb crystals of trapped ions provide a connection between the simple, but not trivial, mathematical models traditionally considered to study this fundamental open question in the field of nonequilibrium statistical physics [12,13], and the thermal conduction experiments on nanometric systems of reduced dimensionality that can be performed nowadays [1,2,17–20].

Experimentally, Coulomb crystals of trapped ions have become an appealing system due to the feasible and unique control of the spatial conformation of ions by adjusting the trap parameters [21–28]. Thus, under very strong trapping conditions the ions exhibit an inhomogeneous alignment along the axial direction [29], whereas a decrease in the transverse trap confinement triggers structural phase transitions in which ions can arrange in flat zigzag or elliptical configurations [21–23,30–32]. Also the formation of three-dimensional helical or spheroidal configurations has been reported [22,33,34].

Another attractive aspect of trapped ion systems is that typical separations between ions of the order of several microns make it possible to focus laser beams on individual ions, which is particularly convenient when designing an energy conduction experiment [1,2].

From a theoretical point of view, trapped ion systems provide a versatile playground for studying energy transport in both classical and quantum regimes [1–11]. To our knowledge, so far the studies have dealt with Coulomb crystals containing a single ion species. It has been shown that the thermodynamic properties of these systems strongly depend on the ion spatial configuration, resulting from the interplay between the many-body Coulomb interaction and the external substrate potential applied on the trap electrodes. It is known that Coulomb monocystals of trapped ions coupled to different thermal baths in two separate regions can exhibit anomalous heat conduction. Both the temperature profiles and the heat flow are very sensitive to the structural phase transitions that modify the effective dimensionality of the system. The linear chain configuration displays an almost flat temperature profile characteristic of harmonic systems, whereas the zigzag and helical configurations show nonzero temperature gradients in the bulk. On the other hand, heat flux becomes optimal in the linear chain configuration in the proximity of the onset for structural phase configurations to higher dimensional configurations [5,10]. A recent analysis of the connection between heat transport properties and the underlying steady nonequilibrium dynamics has elucidated a striking correlation between the ion delocalization and the emergence of nonzero temperature gradients in the two- and three-dimensional configurations [10].

In this work we study energy transport in Coulomb crystals containing two different ion species. Unlike crystals

composed of a single type of ion, in bicrystals the explicit dependence of the trap frequencies on the mass of confined ions must be explicitly taken into account. The mass dependence of the effective trapping frequencies causes simultaneously trapped ion species to experience different confining forces, and as a result the two species may separate spatially [35–38].

We analyze the effects that the mass dependence of the trapping potential has on the steady nonequilibrium dynamics and the kinetic temperature profiles. We will show that the ion delocalization is enhanced by the presence of a heavier ion species in the bicrystal and analyze how the temperature profiles in the bulk are modified according to the masses of the confined ion species. We will consider a three-dimensional model of the trapped bicrystal that fully includes the Coulombian many-body interaction and perform the numerical resolution of the classical Langevin equations. We will set trapping conditions leading to bicrystals that exhibit ion conformations ranging from a string of alternating ions of interest in quantum optics and quantum information processing [39,40] to configurations of higher dimensionality that could be used as sources of atomic or molecular ions for spectroscopy and chemical physics studies and sympathetic cooling [41–44].

The paper is organized as follows. In Sec. II we introduce the model considered to study the nonequilibrium dynamics of bicrystals in contact with two different thermal reservoirs located in separate regions. We describe the details of the numerical experiments and set the parameters corresponding to a possible experimental setup. We consider trapping conditions leading to bicrystals of different dimensionality. In Sec. III we analyze the spatial probability densities of the entire bicrystals and the spatial distributions of the individual ions. The steady kinetic temperature profiles across the axial direction of the trap are analyzed in Sec. IV. To elucidate their behavior on small scales we introduce a model of a Brownian particle confined within a known potential energy surface and interacting with two different thermal reservoirs. Finally, Sec. V summarizes the main conclusions.

## II. THE MODEL

We consider a Coulomb crystal composed of  $N$  ions of two species A and B confined within a radio frequency (rf) trap; the ions of species A has mass  $M_A$  and those of species B mass  $M_B$ . Both ion species have identical charge  $Q$ . We focus on the classical dynamics of the motional degrees of freedom of the ions, described by the position coordinates  $\mathbf{q}_i = (q_{x,i}, q_{y,i}, q_{z,i})$  and their conjugated momenta  $\mathbf{p}_i = (p_{x,i}, p_{y,i}, p_{z,i})$ , with  $i = 1, \dots, N$ .

We assume that the ions interact with each other through the Coulomb repulsion

$$U(|\mathbf{q}_i - \mathbf{q}_j|) = \left( \frac{Q^2}{4\pi\epsilon_0} \right) \frac{1}{|\mathbf{q}_i - \mathbf{q}_j|}, \quad (1)$$

with  $\epsilon_0$  the vacuum permittivity. In current experimental setups the entire ion ensemble can be confined within the finite volume delimited by the spatial distribution of electrodes in radio frequency traps. To achieve such confinement a combination of static and alternating electric fields are applied to the different electrodes [21,45–48]. Here we consider that this

external potential has the form [49,50]

$$V(q_x, q_y, q_z, t) = Q\kappa [V_{\text{dc}}(\Lambda_x q_x^2 + \Lambda_y q_y^2 + \Lambda_z q_z^2) + V_{\text{rf}}(\Lambda'_x q_x^2 + \Lambda'_y q_y^2 + \Lambda'_z q_z^2) \cos(\Omega t)], \quad (2)$$

where  $V_{\text{dc}}$  and  $V_{\text{rf}}$  are the amplitudes of the dc potential and rf driving potential applied to the trap electrodes, respectively;  $\Omega$  is the rf drive frequency; and  $\kappa$  is a constant related to the geometry of the trap electrodes. The parameters  $(\Lambda_x, \Lambda_y, \Lambda_z)$  and  $(\Lambda'_x, \Lambda'_y, \Lambda'_z)$ , which are also determined by the trap geometry, satisfy the Laplace condition

$$\Lambda_x + \Lambda_y + \Lambda_z = \Lambda'_x + \Lambda'_y + \Lambda'_z = 0. \quad (3)$$

We assume appropriate choices of the trap parameters, with  $V_{\text{dc}} \ll V_{\text{rf}}$  and a high-frequency  $\Omega$ , and make use of the pseudopotential approximation to describe the dynamics of trapped ions located sufficiently far away from the trap electrodes and with low kinetic energy. Under these conditions, the trapping potential (2) acting on a trapped ion of mass  $M$  and charge  $Q$  can be replaced by the time-averaged harmonic potential [49]

$$V_{\text{sec}}(q_x, q_y, q_z) = \frac{M}{2} (\omega_x^2 q_x^2 + \omega_y^2 q_y^2 + \omega_z^2 q_z^2), \quad (4)$$

where the secular frequencies

$$\omega_\beta = \sqrt{\frac{2Q}{M} \kappa V_{\text{dc}} \Lambda_\beta + \frac{2Q^2}{M^2 \Omega^2} \kappa^2 V_{\text{rf}}^2 \Lambda_\beta'^2}, \quad (5)$$

with  $\beta = \{x, y, z\}$ , depend both on the charge and on the mass of the trapped ion. Hence, simultaneously trapped ion species of different masses will experience different harmonic confinement frequencies. Specifically, the lighter ion species will be more strongly confined than the heavier one.

Then the dynamics of the two-species ion ensemble ruled by the Coulomb repulsion (1) and the effective harmonic trapping potential (4) can be described by the Hamiltonian

$$H = \sum_{i=1}^N \left[ \frac{\mathbf{p}_i^2}{2M_i} + \frac{1}{2} \sum_{j \neq i}^N U(|\mathbf{q}_i - \mathbf{q}_j|) + V_{\text{sec}}(\mathbf{q}_i) \right]. \quad (6)$$

### A. Nonequilibrium dynamics

We analyze the response of the trapped bicrystal to a imposed temperature gradient, as a function of the masses of the two ion species and the amplitude of the potentials applied to the trap electrodes. To induce heat transport through the ion system, we consider the interaction with two different thermal reservoirs located at both ends of the axial  $x$  direction. To emulate these reservoirs we consider laser beams tuned to act on the ions of species A whenever they visit these regions, whereas the ions of species B are not connected to these laser reservoirs. The two ion species interact with each other through Coulomb repulsion. To characterize the spatial distribution of the laser reservoirs acting on any given ion of species A located at the axial  $x$ -coordinate we introduce the function

$$\mathcal{B}(x; B_L, B_R) = \frac{1}{2} (B_L \{1 - \tanh[a_{\mathcal{B}}(x + x_{\mathcal{B}})]\} + B_R \{1 + \tanh[a_{\mathcal{B}}(x - x_{\mathcal{B}})]\}). \quad (7)$$

Then, for a high-enough value of the parameter  $a_{\mathcal{B}}$ , the ion interacts with the laser reservoir located at the left (L) end whenever  $x \lesssim -|x_{\mathcal{B}}|$ , whereas it is connected to the reservoir located at the right (R) end provided  $x \gtrsim |x_{\mathcal{B}}|$ . The ion is not directly connected to any bath in the intermediate region in which  $-|x_{\mathcal{B}}| \lesssim x \lesssim |x_{\mathcal{B}}|$ . The parameters  $B_L$  and  $B_R$  quantify the coupling to the corresponding bath and determine their effective temperatures.

Assuming that the laser beams behave as Langevin thermal reservoirs, and considering that the typical separations among the ions are of the order of micrometers, we adopt a classical description of the dynamics and express the equations of motion for the  $\alpha = (x, y, z)$  components of the position and momentum coordinates of a given ion of mass  $M_i$  as:

$$\begin{aligned} \dot{q}_{\alpha,i} &= \frac{p_{\alpha,i}}{M_i}, \\ \dot{p}_{\alpha,i} &= g_{\alpha,i} + \sum_{j \neq i}^N f_{\alpha}^{(ij)} - \Theta_i \left[ \mathcal{B}(q_{x,i}; \eta_{\alpha,i}^L, \eta_{\alpha,i}^R) \frac{p_{\alpha,i}}{M_i} \right. \\ &\quad \left. - \mathcal{B}(q_{x,i}; \varepsilon_{\alpha,i}^L(t), \varepsilon_{\alpha,i}^R(t)) \right] \quad \text{for } i = (1, \dots, N), \end{aligned} \quad (8)$$

where  $g_{\alpha,i} = -\partial V_{\text{sec}}(\mathbf{q}_i)/\partial q_{\alpha,i}$  is the external trapping force along the  $\alpha$  direction and  $f_{\alpha}^{(ij)} = -f_{\alpha}^{(ji)} = -\partial U(|\mathbf{q}_i - \mathbf{q}_j|)/\partial q_{\alpha,i}$  the Coulomb repulsion that the  $j$ th ion exerts on the  $i$ th ion along such direction. The function  $\Theta_i = 1(0)$  for ions of the species A (B) has been introduced to differentiate the action of the laser reservoirs between the two ion species.

The interaction with the Langevin reservoirs is characterized by the friction coefficients  $\eta_{\alpha,i}^{L,R}$  and the stochastic forces  $\varepsilon_{\alpha,i}^{L,R}(t)$ . This force is assumed to correspond to a Gaussian white noise that satisfies the statistical relationships

$$\begin{aligned} \langle \varepsilon_{\alpha,i}^{L,R}(t) \rangle &= 0, \\ \langle \varepsilon_{\alpha,i}^{L,R}(t) \varepsilon_{\beta,j}^{L,R}(t') \rangle &= 2D_{\alpha,i}^{L,R} \delta_{\alpha,\beta} \delta_{i,j} \delta(t - t'), \end{aligned} \quad (9)$$

where  $\langle \dots \rangle$  denote the average over an ensemble of stochastic trajectories and  $D_{\alpha,i}^{L,R}$  are the diffusion coefficients. According to the fluctuation dissipation theorem  $D_{\alpha,i}^{L,R} = k_B \eta_{\alpha,i}^{L,R} T^{L,R}$ , with  $T^{L,R}$  the temperature of the corresponding thermal reservoir.

In terms of the friction and diffusion coefficients the equations of motion (8) can be written as the following stochastic differential equations:

$$\begin{aligned} dq_{\alpha,i} &= \frac{p_{\alpha,i}}{M_i} dt, \\ dp_{\alpha,i} &= \left[ g_{\alpha,i} + \sum_{j \neq i}^N f_{\alpha}^{(ij)} - \Theta_i \mathcal{B}(q_{x,i}; \eta_{\alpha,i}^L, \eta_{\alpha,i}^R) \frac{p_{\alpha,i}}{M_i} \right] dt \\ &\quad + \Theta_i \mathcal{B}(q_{x,i}; \sqrt{2D_{\alpha,i}^L}, \sqrt{2D_{\alpha,i}^R}) dW_{\alpha,i} \\ &\quad \text{for } i = (1, \dots, N), \end{aligned} \quad (10)$$

where  $dW_{\alpha,i}$  denote the Wiener processes associated with the interactions with the laser reservoirs.

For small laser intensities, the friction coefficients  $\eta_{\alpha,i}^{L,R}$  and the diffusion coefficients  $D_{\alpha,i}^{L,R}$  can be obtained from the Doppler cooling expressions [51]:

$$\eta_{\alpha,i}^{L(R)} = -4\hbar [k_{\alpha,i}^{L(R)}]^2 \frac{\left[ \frac{I_{\alpha,i}^{L(R)}}{I_0^{L(R)}} \right]}{\left\{ 1 + 4 \left[ \frac{\delta_{\alpha,i}^{L(R)}}{\Gamma} \right]^2 \right\}^2} \quad (11)$$

and

$$D_{\alpha,i}^{L(R)} = \hbar^2 [k_{\alpha,i}^{L(R)}]^2 \frac{\left[ \frac{I_{\alpha,i}^{L(R)}}{I_0^{L(R)}} \right]}{\left\{ 1 + 4 \left[ \frac{\delta_{\alpha,i}^{L(R)}}{\Gamma} \right]^2 \right\}} \Gamma. \quad (12)$$

The ratio  $I_{\alpha,i}^{L(R)}/I_0^{L(R)}$  denotes the normalized intensity of the laser beam acting on the  $i$ th ion along the  $\alpha$  direction,  $k_{\alpha,i}^{L(R)}$  is the corresponding laser wavenumber,  $\delta_{\alpha,i}^{L(R)} = \omega_{\alpha,i}^{L(R)} - \omega_0$  is the detuning of the laser frequency  $\omega_{\alpha,i}^{L(R)}$  with respect to the frequency  $\omega_0$  of a selected atomic transition in the ion, and  $\Gamma$  is the natural linewidth of the excited state in such transition.

## B. Numerical experiments

In this work we consider bicrystals containing  $\text{Mg}^+$  ions, which correspond to the species A that is connected to the thermal reservoirs, and different ions of species B. For these ions we select  $\text{Ca}^+$ ,  $\text{Zn}^+$ , and  $\text{Sr}^+$ . Then in the three bicrystals the ions of species B are heavier than those of species A.

The Doppler cooling associated with the thermal reservoirs is applied to the atomic transition  $3s^2S_{1/2} \rightarrow 3p^2P_{3/2}$  of the  $^{24}\text{Mg}^+$  ions, with  $\omega_0/2\pi = 1072$  THz and  $\Gamma/2\pi = 42.669$  MHz [35]. To induce heat transport through the axial direction we consider that the laser reservoirs located at both ends have different detunings  $\delta_{\alpha,i}^L \neq \delta_{\alpha,i}^R$ . Considering the dependence of the limit temperature in the Doppler cooling with the laser detuning, in order to generate an appreciable difference of temperature between both laser reservoirs we fix the detuning in one of them sufficiently small. In the numerical simulations we set  $\delta_{\alpha,i}^L = -0.02\Gamma$  for the left reservoir located at  $x \lesssim -|x_{\mathcal{B}}|$  and  $\delta_{\alpha,i}^R = -0.1\Gamma$  for the right reservoir located at  $x \gtrsim |x_{\mathcal{B}}|$ . We consider the same laser intensity  $I_{\alpha,i}^{L(R)}/I_0^{L(R)} = 0.08$  on both reservoirs. The corresponding friction coefficients are  $\eta^L = 6.79 \times 10^{-22}$  kg/s and  $\eta^R = 3.15 \times 10^{-21}$  kg/s and the diffusion coefficients  $D^L = 1.20 \times 10^{-46}$  kg<sup>2</sup>m<sup>2</sup>/s<sup>3</sup> and  $D^R = 1.16 \times 10^{-46}$  kg<sup>2</sup>m<sup>2</sup>/s<sup>3</sup>. In the case of the laser cooling of a single isolated  $^{24}\text{Mg}^+$  ion, the resulting limit Doppler temperatures are  $T^L = D^L/k_B\eta^L = 12.82$  mK and  $T^R = D^R/k_B\eta^R = 2.66$  mK. Thus in the bicrystals the ions of species A will be connected to an effective hotter bath on the left end and to a colder bath on the right end.

To perform the numerical simulations, from now on we will consider a system composed of  $N = 31$  ions, with 18 of them of species A ( $\text{Mg}^+$ ) and the remaining 13 of species B ( $\text{Ca}^+$ ,  $\text{Zn}^+$ ,  $\text{Sr}^+$ ). The spatial distribution of the laser reservoirs is set by the parameters  $a_{\mathcal{B}} = 1.0 \times 10^7 \mu\text{m}^{-1}$  and  $x_{\mathcal{B}} = 160 \mu\text{m}$ . To fix the initial conditions of the ions, we consider a sequence of  $N$  small boxes centered along the axial  $x$  direction so that each ion is initially at rest in a random position inside one of these boxes. At both ends of the system we place 3 boxes within the region  $|x| > |x_{\mathcal{B}}|$  where the



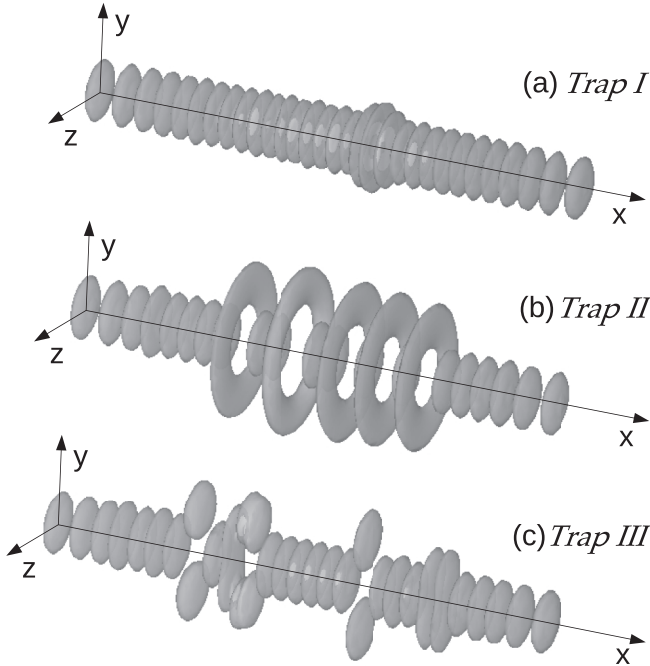


FIG. 3. Spatial probability density  $P(\mathbf{q})$  [Eq. (13)] of the  $\text{Mg}^+\text{-Zn}^+$  bicrystal in (a) Trap I, (b) Trap II, and (c) Trap III, obtained from a single stochastic realization. The positions  $\mathbf{q}$  with values of  $P(\mathbf{q})$  below 5% of its maximum value are not depicted. The total extension of the system along the axial direction is approximately  $420 \mu\text{m}$  in Trap I,  $396 \mu\text{m}$  in Trap II, and  $422 \mu\text{m}$  in Trap III. Notice that in Trap III the ions are confined in the  $xy$  plane. In the numerical simulations we set  $t = \tau_{\text{ss}} = 0.1 \text{ s}$  and  $\sigma = 2 \mu\text{m}$ . The VESTA software was used for the visualization of the spatial distributions [52].

#### A. The same bicrystal in different trapping conditions

Figure 3 shows the steady-state spatial probability densities (13) of the entire  $\text{Mg}^+\text{-Zn}^+$  bicrystal in the three traps, obtained from a single stochastic trajectory. The details of these spatial probability densities for different stochastic realizations are not necessarily equally distributed across the trap, but they all exhibit a similar overall qualitative appearance. The different delimited components that make up the global distribution do not necessarily correspond to specific individual ions but to space regions with a high density of probability of finding the ions during the steady state.

As occurs with monocrystals, the effective dimensionality of the system is determined by the trapping conditions. The strongest transverse confinement in Trap I keeps virtually all ions aligned very close to the axial direction. In this trap the number of discrete dots arranged along the axis coincides with the total number of strongly confined ions in the bicrystal. Similarly to what has been observed in monocrystals, the decrease in the transverse confinement induces structural phase transitions in which the ions can adopt two-dimensional and three-dimensional spatial configurations. The symmetrical decrease of the two radial frequencies in Trap II results in the emergence of a series of rings contained in the transverse plane and centered along the  $x$  direction. Here again each of the discrete dots arranged along the axial axis can be assigned

to a localized individual ion, whereas each of the rings can contain more than one delocalized ion orbiting around that axis. These rings are similar to those associated with the helical configuration in monocrystals. Although unlike what happens in such systems, in bicrystals there are ions that are still confined on the axial axis in between the rings.

In Trap III the asymmetric decrease of the radial frequencies triggers a structural phase transition to a two-dimensional configuration in which ions dynamics is restricted to the plane perpendicular to the transverse direction with the highest trapping frequency. Some ions appear symmetrically arranged on both sides of the axial axis, which is reminiscent of the zigzag configuration observed in monocrystals. Although unlike what happens in such systems, in the bicrystals the two-dimensional configuration does not necessarily emerges in the center where now there are still ions that persist aligned on the axial axis.

In order to differentiate the dynamics of the two ionic species in the bicrystal, we now analyze the steady spatial distribution of the individual ions. Specifically, we consider the spatial distribution of each  $i$ th ion along the  $\alpha$  direction given by [10]

$$\begin{aligned} \Theta_i(\alpha) &\equiv \Theta_i(\alpha_l) \\ &= \frac{1}{\tau_{\text{ss}}} \left\langle \int_t^{t+\tau_{\text{ss}}} d\tau \int_{\alpha_l-\Delta/2}^{\alpha_l+\Delta/2} d\alpha \delta[\alpha - q_{\alpha,i}(\tau)] \right\rangle, \end{aligned} \quad (14)$$

where  $\alpha_l$  and  $\Delta$  are the location of the center and the size of a given spatial cell along such direction, respectively. To obtain a quasicontinuous spatial distribution we set a series of  $c_\alpha$  cells, with  $l = 1, \dots, c_\alpha$ , and a small-enough value of  $\Delta$ .

The radial distributions  $\Theta_i(y)$  and  $\Theta_i(z)$  clearly distinguish between the dynamics of the two ion species in the global spatial probability densities shown in the Fig 3. As Fig. 4 shows, the lighter  $\text{Mg}^+$  ions exhibit a single zero centered peak, indicating that they remain aligned along the axial axis, whereas the heavier  $\text{Zn}^+$  ions can explore the transverse directions as they are subjected to weaker confinement. These are the ions that can experience the structural phase transitions from the nearly string arrangement in Trap I to the three-dimensional configuration exhibited in the symmetrical Trap II and the two-dimensional one observed in the asymmetrical Trap III. In Trap II the identical bimodal distributions in the two radial coordinates, with two peaks of the same intensity arranged symmetrically around zero, is characteristic of the rings giving the helical configuration in monocrystals [10]. Similarly to the zigzag configuration in monocrystals, in Trap III the heavier ions remain confined in the radial direction with the highest trapping frequency and exhibit a bimodal distribution in the other transverse direction of lower confinement. The two major peaks on both sides of the axial axis indicate that the ions remain most of the time in the vicinity of the minima of the global potential energy surface around that axis. Although the small bump at the center of this distribution indicates that these ions can also remain a significant amount of time on the axial axis, something that does not occur in the case of the zigzag configuration of monocrystals [10].

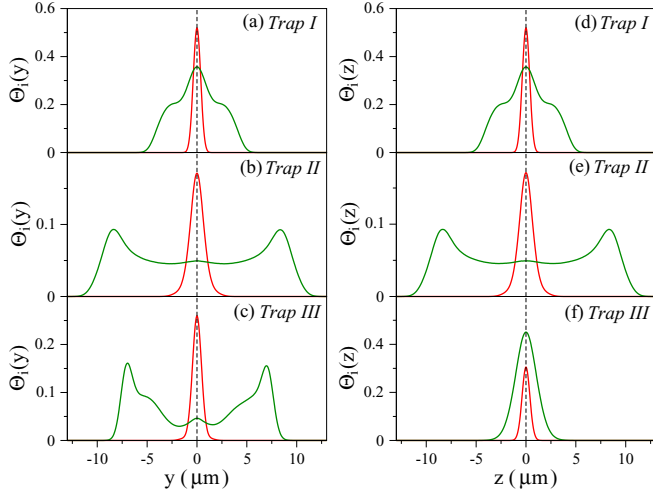


FIG. 4. Steady radial distributions  $\Theta_i(y)$  [(a) Trap I, (b) Trap II, and (c) Trap III] and  $\Theta_i(z)$  [(d) Trap I, (e) Trap II, and (f) Trap III] [Eqs. (14)] corresponding to the same two internal ions of the  $\text{Mg}^+$ - $\text{Zn}^+$  bicrystal in the different traps. The selected ions initially occupy the two central colored positions in Fig. 1. The green line is the central  $\text{Zn}^+$  ion and the red line is the  $\text{Mg}^+$  ion to the right of such central ion. We consider  $c_y = c_z = 1000$  cells with size  $\Delta = 0.04 \mu\text{m}$  along both radial directions, set the time values  $t = \tau_{\text{ss}} = 0.1$  s, and average over more than 400 stochastic trajectories. For a better analysis, the intensity of the peaks of the  $\text{Zn}^+$  ion distribution has been multiply by a factor of 4 in all the panels.

### B. Different bicrystals in the same trapping conditions

So far we have analyzed the dynamics of a given bicrystal in different trapping conditions. We now consider bicrystals containing the same species A but different species B confined in identical traps. We study the effects of the mass dependence of the trapping frequencies on the dynamics.

Figure 5 shows the steady spatial distributions  $\Theta_i(\alpha)$  [Eq. (14)] for several individual ions of the  $\text{Mg}^+$ - $\text{Ca}^+$ ,  $\text{Mg}^+$ - $\text{Zn}^+$ , and  $\text{Mg}^+$ - $\text{Sr}^+$  bicrystals confined in the symmetrical Trap II.

$$T(\alpha) \equiv T(\alpha_i) = \frac{2}{3k_B} \frac{\left\langle \sum_{i=1}^N \int_t^{t+\tau_{\text{ss}}} d\tau \int_{\alpha_i-\Delta/2}^{\alpha_i+\Delta/2} d\alpha \delta(\alpha - q_{\alpha,i}(\tau)) E_k(\mathbf{p}_i(\tau)) \right\rangle}{\left\langle \sum_{i=1}^N \int_t^{t+\tau_{\text{ss}}} d\tau \int_{\alpha_i-\Delta/2}^{\alpha_i+\Delta/2} d\alpha \delta(\alpha - q_{\alpha,i}(\tau)) \right\rangle}, \quad (15)$$

where  $E_k(\mathbf{p}_i)$  is the kinetic energy of the  $i$ th ion and  $k_B$  the Boltzmann constant.

Figure 6 shows the axial kinetic temperature profiles for the  $\text{Mg}^+$  monocrystal and the different bicrystals confined in the symmetrical Trap II and the asymmetrical Trap III. Due to the small size of the systems the temperature profiles display significant boundary effects, mainly in the outermost locations where the laser reservoirs are acting and in their adjacent regions. We focus on the analysis of the temperature profile in the central region where it becomes strongly sensitive to the mass of the heavier ion species. Within this region

Similarly to the zigzag and helical distributions in monocrystals [10], the distributions  $\Theta_i(x)$  evidence a significant delocalization of the internal ions of both species along the axial axis of the trap. The series of peaks of the lighter ions of species A indicate that they can exchange their positions along this axis, whereas the more widespread distributions of the heavier ions of species B correspond to the delocalization of these ions along the series of external rings arranged around the axial axis, see Fig. 3. The increase in the mass of the ion of species B contributes to increase the delocalization of the ions of both species, which can thus explore a larger portion of the axial region encompassed by the entire trapped system. This increased axial delocalization of ions may eventually be responsible for the ions of species A leaving the spatial region in which the laser reservoirs are acting.

The analysis of the spatial distributions  $\Theta_i(y)$  and  $\Theta_i(z)$  shows that the increase in the mass of the ions of species B also leads to a greater transverse delocalization of these ions, which in a symmetrical trap occupy rings of an ever-increasing radius. Whereas the lighter ions of species A are increasingly confined on the axial axis, see Fig. 5. Therefore, the increase in the mass of the ions of species B contributes to making the spatial segregation of the two ion species more significant due to the mass dependence of the trapping frequencies.

### IV. TEMPERATURE PROFILES

In this section we analyze the effect of the mass dependence of the trapping frequencies on the steady-state temperature profiles across bicrystals in which ions of the species A can interact with different laser reservoirs that are located at both ends of the axial direction, see Fig. 1. The kinetic temperatures can be obtained from the momentum coordinates  $\{\mathbf{p}\}_N = (\mathbf{p}_1, \dots, \mathbf{p}_N)$  of the ions in the nonequilibrium steady state reached under the action of the two thermal reservoirs.

Taking into account the possible ion delocalization for certain trapping conditions, we consider a continuous description to define the steady local kinetic temperature  $T(x)$  across the axial direction in terms of the equipartition theorem as [10]:

the kinetic temperature changes from a nearly flat profile in the  $\text{Mg}^+$  monocrystal to profiles with nonzero gradients in the bicrystals. Similarly to monocrystals [10], the delocalized dynamics of the heavier ions across the rings in the symmetrical traps results in temperature profiles with uniform gradients, whereas their delocalization in the planar zigzag type configurations of the asymmetrical traps corresponds to nonfully linear temperature profiles. Both in the symmetrical and asymmetrical traps the magnitude of the temperature gradient becomes larger with the increase of the mass of the heavier ion species. In the case of the asymmetrical trap the

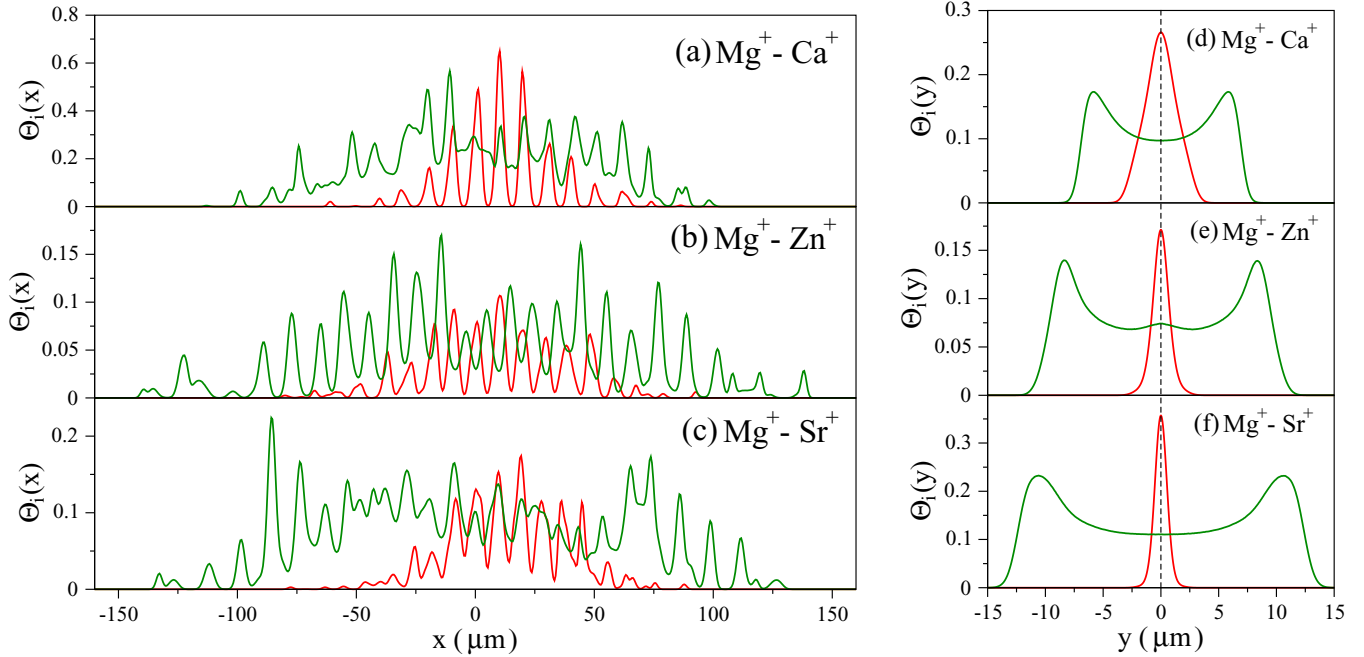


FIG. 5. Left: Steady longitudinal distribution  $\Theta_i(x)$  [Eqs. (14)] for the same two ions of the (a)  $\text{Mg}^+ - \text{Ca}^+$ , (b)  $\text{Mg}^+ - \text{Zn}^+$ , and (c)  $\text{Mg}^+ - \text{Sr}^+$  bicrystals confined in Trap II. The colors of the two lines correspond to the colored ions in Fig. 1. The green line is the ion of species B ( $\text{Ca}^+$ ,  $\text{Zn}^+$ ,  $\text{Sr}^+$ ) that initially occupies the central location in the system. The ion of species A ( $\text{Mg}^+$ ) that is initially to the right of this central ion correspond to the red line. For a better analysis, the intensity of the peaks of the ions of species B has been multiply by a factor of 3 in the three bicrystals. Right: Steady radial distribution  $\Theta_i(y)$  (14) for the two ions considered in the left panel for the (d)  $\text{Mg}^+ - \text{Ca}^+$ , (e)  $\text{Mg}^+ - \text{Zn}^+$ , and (f)  $\text{Mg}^+ - \text{Sr}^+$  bicrystals confined in Trap II. Due to the axial symmetry both radial distributions  $\Theta_i(y)$  and  $\Theta_i(z)$  coincide. The same line colors are used as in the left panel. For a better analysis, the intensity of the peaks of the ion of species B has been multiply by a factor of 2 in the  $\text{Mg}^+ - \text{Ca}^+$  bicrystal, a factor of 6 in the  $\text{Mg}^+ - \text{Zn}^+$  bicrystal, and a factor of 8 in the  $\text{Mg}^+ - \text{Sr}^+$  bicrystal. We consider  $c_x = c_y = c_z = 1000$  cells, with size  $\Delta = 0.5 \mu\text{m}$  along the axial direction and size  $\Delta = 0.04 \mu\text{m}$  along the radial directions. In the numerical simulations we set the time values  $t = \tau_{ss} = 0.1$  s and average over more than 400 stochastic trajectories.

temperature profile also bends further within the small size of the system, see Fig. 6.

Similarly to monocrystals [10], these results reveal a direct correlation between temperature profile through the axial direction and the amount of ion delocalization within the trap.

In monocrystals delocalization emerges due to changes in trapping conditions by decreasing the transverse frequencies, whereas for a given trap with fixed secular frequencies, we have just shown that an analogous delocalization arises when considering bicrystals containing heavier ion species. The

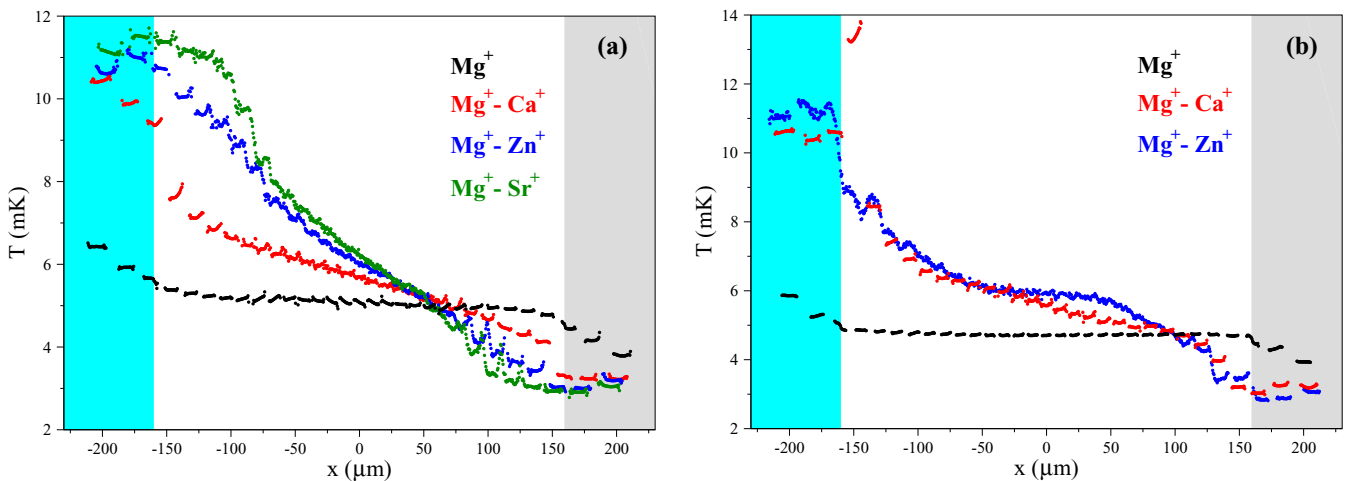


FIG. 6. The steady-state kinetic temperature profiles  $T(x)$  [Eq. (15)] across the axial direction for the  $\text{Mg}^+$  monocrystal and the different bicrystals confined in (a) Trap II and (b) Trap III. The colored areas are the regions where the two laser reservoirs are acting. The results were obtained from the numerical simulation of the dynamics in the interval  $[0.1, 0.2]$  s of the steady state and the average over more than 600 stochastic trajectories.

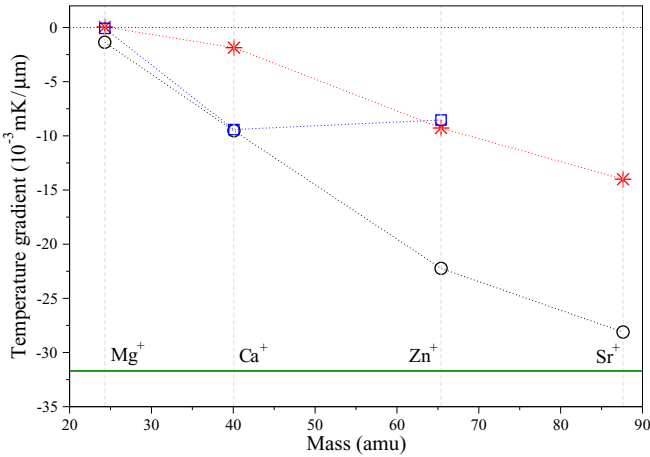


FIG. 7. Central gradient of the axial temperature profile for the  $\text{Mg}^+$  monocrystal and the  $\text{Mg}^+\text{-Ca}^+$ ,  $\text{Mg}^+\text{-Zn}^+$ , and  $\text{Mg}^+\text{-Sr}^+$  bicrystals confined in Traps I, II, and III, as a function of the  $\text{Mg}^+$  ion mass in the monocrystal and the mass of the ion of the species B in the bicrystals. The central gradients were obtained from the slopes of the corresponding temperature profiles in the axial interval  $[-100, 100]$   $\mu\text{m}$ . The green horizontal line corresponds to the Fourier temperature gradient given by  $(T^R - T^L)/2x_{\mathcal{B}}$ . The same symbols as in Fig. 2 have been used to denote the different traps. Dashed lines are drawn to guide the eye.

magnitude of the temperature gradient increases as the range of delocalization of internal ions continues to expand and tends to stabilize once it covers the entire space available to the trapped system.

To summarize, we now analyze the central gradient of the axial temperature profile in the  $\text{Mg}^+$  monocrystal and the different bicrystals in the three traps, see Fig. 7. In the case of the  $\text{Mg}^+$  monocrystal, the transverse frequencies in Traps I and III are high enough to keep all the ions tightly confined around their equilibrium positions along the axial axis, and, consequently, this system displays an almost zero temperature gradient [5,10], whereas the small nonzero temperature gradient of this monocrystal in the weaker confinement of Trap II emerges from the ion delocalization across the helical configuration [10]. A very small temperature gradient is also observed in the  $\text{Mg}^+\text{-Ca}^+$  bicrystal confined in Trap I, in which both ion species remain strongly confined along the axial axis according to the fixed initial ion conformation shown in Fig. 1. The noticeable nonzero temperature gradients emerge with the ion delocalization under weaker trapping conditions and/or in bicrystals with heavier species B ions.

The three traps evidence a direct correspondence between the magnitude of the central temperature gradient and the amount of ion delocalization. So the more delocalized the ions are in the trap, the larger the magnitude of such gradient. In the case of the two symmetrical traps, the weaker confinement in Trap II results in a higher ion delocalization of the heavier ion species within all bicrystals, both in the axial and transverse directions, and therefore the magnitude of the temperature gradients is larger than those of Trap I. Also, the bicrystal with the heaviest ion species confined in Trap II, which is

the system that exhibits the highest ion delocalization, is the one with the central temperature gradient closest to value  $(T^R - T^L)/2x_{\mathcal{B}}$  predicted by a Fourier-type behavior, see Fig. 7.

The observed increase in the magnitude of the temperature gradient with a higher ion delocalization occurs provided the trapping conditions are strong enough to keep ions of species A at the ends of the system where the thermal reservoirs are acting. This may not happen in bicrystals containing very heavy ions and/or in traps with very weak confinement, due to the displacement of the ions of species B toward both ends where the laser reservoirs that act on the ions of species A are located. Then due to Coulombian repulsion, these lighter ions are forced to move toward the internal region where they do not interact with the thermal reservoirs. When this occurs the system no longer has the necessary configuration for a heat conduction process to be established. This effect, which has been already observed in the case of the  $\text{Mg}^+\text{-Sr}^+$  bicrystal confined in the asymmetrical Trap III, is expected to eventually occur also in symmetrical traps. Although for bicrystals with much heavier B species ions, as they could reach the delocalization necessary for this to happen.

In the asymmetric Trap III, the apparent decrease in the magnitude of the temperature gradient in the  $\text{Mg}^+\text{-Zn}^+$  bicrystal, with respect to value obtained in the more localized  $\text{Mg}^+\text{-Ca}^+$  bicrystal, is only due to the bending of the temperature profile characteristic of planar configurations, see Fig. 6. For larger systems this effect would become less relevant, so that the predicted increase in magnitude of the temperature gradient associated with a higher ion delocalization would be observed.

An interesting issue is to analyze the dependence of the behavior of the kinetic temperature profiles on the parameters that define the interaction with the thermal baths. Figure 8 shows the variation of the temperature profile of the  $\text{Mg}^+\text{-Ca}^+$  bicrystal confined in Trap II as the laser intensity corresponding to the R-bath of the coldest temperature changes. We consider intensities sufficiently small so that the Doppler cooling expressions Eqs. (11) and (12) can be applied. According to these expressions, a decrease in the laser intensity decreases both the friction coefficient  $\eta^R$  and the diffusion coefficient  $D^R$  while the temperature limit  $T^R$  is not modified. As the temperature profile through the system results from the combined action of the two thermal baths, the weaker coupling of the ions to the colder bath reinforces the effect of the hotter one. Thus, the temperature of the ions increases. Also, this increase makes the boundary effects more significant in the proximity of the coldest bath, where the gap between the temperatures of the most external ions that are coupled to the laser reservoirs and the temperatures of their closest internal neighbors becomes larger, while, on the other hand, such gap is being reduced in the boundary of the hotter bath. As a result, the central gradient of the axial temperature profile decreases slightly as the coupling to the colder bath becomes weaker, see Fig. 8. Both the monocrystal and the different bicrystals exhibit similar behavior. Thus, the differences between the central temperature gradients of the different ion species shown in Fig. 7 are robust to changes in the strength of the coupling to the thermal reservoirs.

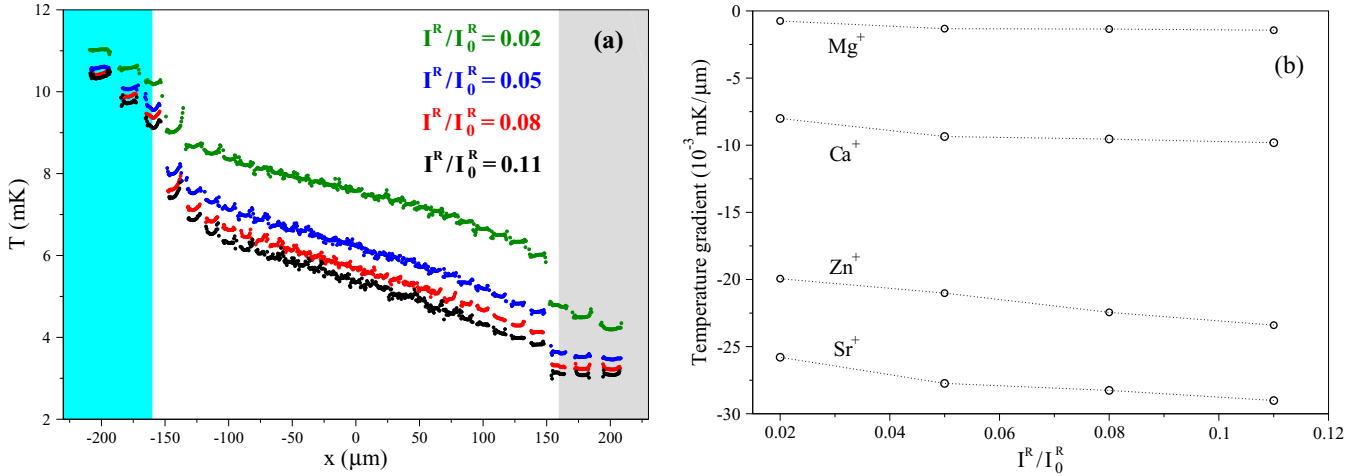


FIG. 8. (a) The steady-state kinetic temperature profiles  $T(x)$  [Eq. (15)] across the axial direction for the  $\text{Mg}^+$ - $\text{Ca}^+$  bicrystal confined in Trap II for different laser intensities  $I^R/I_0^R$ . The remaining parameters are the same as in Fig. 6. (b) Central gradient of the axial temperature profile for the  $\text{Mg}^+$  monocrystal and the  $\text{Mg}^+$ - $\text{Ca}^+$ ,  $\text{Mg}^+$ - $\text{Zn}^+$ , and  $\text{Mg}^+$ - $\text{Sr}^+$  bicrystals confined in Trap II as a function of the laser intensity  $I^R/I_0^R$ . The gradients were obtained as in Fig. 7. Dashed lines are drawn to guide the eye.

### A. Local kinetic temperature on small scales

Once the global behavior of the steady kinetic temperature profiles along the axial direction has been analyzed for several bicrystals confined in different trapping conditions, we now analyze their structure on small scales. As Fig. 9 shows, there is clear correlation between the behavior of the kinetic temperature  $T(x)$  [Eq. (15)] and the total spatial distribution

$$\Xi(x) = \sum_{i=1}^N \Theta_i(x), \quad (16)$$

and the total kinetic energy distribution

$$\varepsilon_k(x) = \frac{1}{\tau_{\text{ss}}} \left\langle \sum_{i=1}^N \int_t^{t+\tau_{\text{ss}}} d\tau \int_{\alpha_i - \Delta/2}^{\alpha_i + \Delta/2} d\alpha \delta[\alpha - q_{\alpha,i}(\tau)] E_k[\mathbf{p}_i(\tau)] \right\rangle \quad (17)$$

of the ions through the axial direction of the trap.

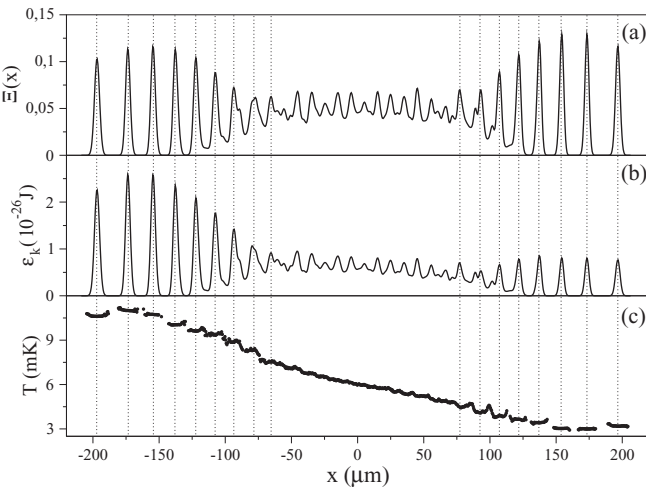


FIG. 9. (a) Total steady longitudinal distribution  $\Xi(x)$  [Eq. (16)], (b) total steady kinetic energy distribution  $\varepsilon_k(x)$  [Eq. (17)], and (c) and the steady kinetic temperature profile  $T(x)$  [Eq. (15)] for the  $\text{Mg}^+$ - $\text{Zn}^+$  bicrystal confined in Trap II.

At both ends of the system the temperature profile displays a series of separate small segments centered in each of the locations of ion confinement. The span of each segment is determined by the size of the corresponding peak in the spatial distribution. At the center of the segments, where the spatial distribution is maximum, the temperature value tends to stabilize, while it presents variations in the edges of each segment as the probability of presence of ions decreases sharply. The empty spaces between the most external segments correspond to positions that are not visited by the ions during the dynamics.

As the axial coordinate moves toward the center of the chain, the probability of presence of ions between the peaks of the spatial distribution begins to be significant due to their increasing delocalization. In this intermediate region of the system, the partial overlap of the edges of adjacent segments results in an oscillating kinetic temperature profile at small scales. Thus, these small variations of the kinetic temperature evidence the incipient transit of delocalized ions between two neighboring local confinement regions across the axial direction of the trap. They are analog to the variations in the temperature profiles reported in the analysis of heat transport in polygonal billiards that confine freely evolving particles [53,54] rather than being similar to the oscillating temperature profiles observed in Fermi-Pasta-Ulam chains with alternating light and heavy masses, which are strongly confined around their equilibrium positions [55,56]. As Fig. 9 shows, in trapped ion systems the oscillation at small scales fades and the temperature profile smooths in the vicinity of the center of the system, as the spatial distribution of the ions becomes increasingly uniform due to their widespread delocalization across the axial direction of the trap.

Considering that the locations of maximum probability of presence of ions are also those of maximum kinetic energy, see Fig. 9, they must also correspond to the locations of the local minima of the potential energy surface that confines the system. Thus, the behavior of the local kinetic temperature on small scales is determined by the spatial distribution of

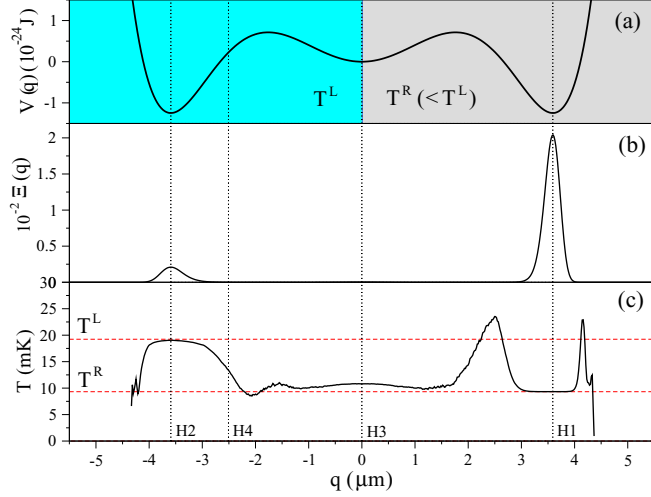


FIG. 10. (a) The potential energy surface  $V(q)$  [Eq. (18)], with the parameters  $c_6 = 2.5 \times 10^{10} \text{ Jm}^{-6}$ ,  $c_4 = -0.4 \text{ Jm}^{-4}$ , and  $c_2 = 1.0 \times 10^{-18} \text{ Jm}^{-2}$ . The colored regions denote the spatial distribution of the two thermal reservoirs, located at  $q \lesssim 0$  (L) and  $q \gtrsim 0$  (R). (b) Steady spatial distribution of a Brownian particle with the mass  $M$  of the  $\text{Mg}^+$  ion, confined within the potential energy surface (a) and coupled to the two thermal reservoirs. To establish the interaction with the two Langevin baths we have fixed the friction coefficients  $\eta^L = 6.79 \times 10^{-22} \text{ kg/s}$  and  $\eta^R = 3.15 \times 10^{-22} \text{ kg/s}$ , and the diffusion coefficients  $D^L = 1.80 \times 10^{-46} \text{ kg}^2\text{m}^2/\text{s}^3$  and  $D^R = 4.05 \times 10^{-46} \text{ kg}^2\text{m}^2/\text{s}^3$ . The corresponding limit temperatures are  $T^L = D^L/k_B\eta^L = 19.23 \text{ mK}$  and  $T^R = D^R/k_B\eta^R = 9.32 \text{ mK}$ , respectively. The results were obtained from the numerical simulations of the dynamics in the interval  $[3.84 \times 10^{-3}, 7.68 \times 10^{-3}] \text{ s}$  of the steady state and the average over more than  $3 \times 10^4$  stochastic trajectories. (c) The local kinetic temperature  $T(x)$  [Eq. (15)] corresponding to the numerical simulation described in (b). The red dashed lines indicate the temperatures  $T^L$  and  $T^R$  of the two thermal reservoirs. The vertical dashed lines indicate the position coordinates corresponding to the four histograms shown in Fig. 11.

ions across the surface of the trapping potential, according to the energy supplied by the thermal baths. Specifically, the variations of the kinetic temperature at small scales arise due to the transit of delocalized ions through the different barriers of the interaction potential.

To illustrate the correlation between the behavior of the kinetic temperature on small scales and the spatial delocalization of the particles through the structure of the surface of the trapping potential, next we analyze a simple model that makes it explicit.

### 1. Model: Brownian particle confined in a three-well potential and coupled to two thermal reservoirs

We consider a one-dimensional system composed of a single particle of mass  $M$  and with position coordinate  $q$ , which is confined within the three-well potential energy surface

$$V(q) = c_6 \frac{q^6}{6} + c_4 \frac{q^4}{4} + c_2 \frac{q^2}{2}. \quad (18)$$

The particle is coupled to two different laser reservoirs that are spatially distributed according to the function  $\mathcal{B}(q; B_L, B_R)$  [Eq. (7)], with  $x_{\mathcal{B}} = 0$ , see Fig. 10.

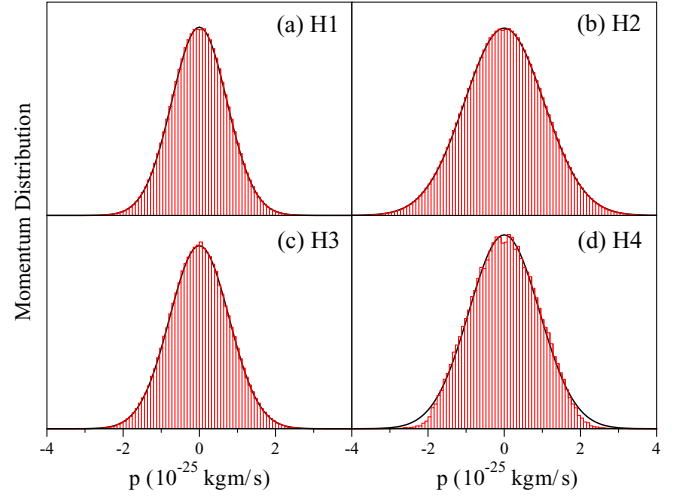


FIG. 11. The histograms (red lines) giving the distribution of the momentum of the particle at different position coordinates and the Gaussian fitting of the data (black lines). The histogram (a) H1 corresponds to the position coordinate  $q = 3.591 \mu\text{m}$ , (b) H2 to  $q = -3.591 \mu\text{m}$ , (c) H3 to  $q = 0 \mu\text{m}$ , and (d) H4 to  $q = -2.508 \mu\text{m}$ . The histograms H1 and H2 were obtained from a data sample of  $3 \times 10^6$  elements, the histogram H3 from 419 016 elements, and the histogram from 77 532 elements.

As in the trapped ion system, we adopt a classical description of the dynamics and assume that the laser beams behave as Langevin thermal reservoirs. Then the equations of motion for the position and momentum coordinates  $(q, p)$  can be written as

$$\begin{aligned} dq &= \frac{p}{M} dt, \\ dp &= \left[ -\frac{\partial V}{\partial q} - \mathcal{B}(q; \eta^L, \eta^R) \frac{p}{M} \right] dt \\ &\quad + \mathcal{B}(q; \sqrt{2D^L}, \sqrt{2D^R}) dW. \end{aligned} \quad (19)$$

As Fig. 10 shows, the confinement of the particle around the positions of the local minima of the potential energy surface leads to plateaus in the kinetic temperature profile. As in the case of the trapped ion system, these plateaus are centered in the positions of greatest probability of presence of the particle and their span is determined by the size of the corresponding peak in the spatial distribution. The tendency of the particle to occupy the positions of the thermal bath with the lowest temperature is reflected in the best definition of the plateau of the temperature corresponding to the potential energy well located in that region. At the unstable coordinates of the dynamics located around the maxima of the barriers of the potential energy surface, where the probability of presence of the particle becomes extremely small, the temperature can exhibit significant variations. Paradoxically, in these regions the local kinetic temperature can even take values that are outside the range set by the temperatures of two thermal reservoirs, see Fig. 10.

An interesting question is whether the differentiated behavior of the kinetic temperature around the stable and unstable points of dynamics is related to the validity of local thermal equilibrium. To analyze this issue we focus on the

TABLE I. The position coordinate  $q$ , the kurtosis  $\kappa$  [Eq. (20)], the kinetic temperature given by the equipartition theorem according to Eq. (15), and the temperature obtained from the fitting of the histograms giving the momentum distributions to the Gaussian canonical distribution  $h(p) \propto e^{-p^2/2Mk_B T}$  for the different histograms shown in Fig. 11.

| Histogram | $q(\mu\text{m})$ | $\kappa$                | $T(\text{mK})$ [Eq. (15)] | $T(\text{mK})$ (canonical distribution) |
|-----------|------------------|-------------------------|---------------------------|-----------------------------------------|
| H1        | 3.591            | $1.107 \times 10^{-3}$  | 9.33                      | 9.39                                    |
| H2        | -3.591           | $-6.442 \times 10^{-2}$ | 19.03                     | 19.40                                   |
| H3        | 0                | $-5.861 \times 10^{-2}$ | 10.83                     | 10.90                                   |
| H4        | -2.508           | -0.424                  | 13.26                     | 15.31                                   |

steady-state distribution of the momentum of the particle at different position coordinates. As is known, in the locations where the local thermal equilibrium is satisfied, such distribution should exhibit a Gaussian profile characteristic of the canonical distribution [57]. Figure 11 shows the histograms that give the momentum distribution at different locations across the structure of the potential energy surface depicted in Fig. 10. The figure also includes the best Gaussian fitting of the data.

As a criterion to quantify the deviation of each momentum distribution from the Gaussian profile of the canonical distribution, we consider the kurtosis [57]

$$\kappa = \frac{\langle (p - \bar{p})^4 \rangle}{\langle (p - \bar{p})^2 \rangle^2} - 3, \quad (20)$$

see Table I. A Gaussian distribution gives  $\kappa = 0$ , whereas  $\kappa > 0$  ( $< 0$ ) corresponds to a distribution with a narrower (wider) central peak and wider (narrower) tails.

In the position coordinates close to the minima of the potential energy surface, where the probability of presence of the particle is significant, both (i) the sufficiently small values of the kurtosis and (ii) the agreement between the kinetic temperature obtained from the equipartition theorem according to Eq. (15) and the value resulting from the Gaussian fitting of the momentum distribution to a function  $h(p) \propto e^{-p^2/2Mk_B T}$  characteristic of the canonical distribution are consistent with local thermal equilibrium, while in the case of the unstable positions of the dynamics around the barriers of the potential, the numerical results indicate that both the kurtosis and kinetic temperature values deviate from those prescribed by local thermal equilibrium. Notice that obtaining conclusive results concerning these unstable regions, where the probability of presence of the particle can be extremely small, becomes a difficult task due to the very scarce data sample that can be extracted from the dynamics to analyze the momentum distribution. This issue requires a further analysis in future work.

To summarize, the analysis of this simple model of a single Brownian particle confined within a known potential energy surface has shed light on the behavior on small scales of kinetic temperature profiles in trapped ion systems. Specifically, their variations at small scales are inherent to the transit of the delocalized ions through the structure of the trapping potential energy surface. The kinetic temperature tends to stabilize around the confinement positions dictated by the local potential wells, where the results are consistent with local thermal equilibrium. While the temperature variations

at small scales occur around the local barriers of the trapping potential where the probability of presence of ions becomes very small. In these regions of instability the analysis of the momentum distribution indicates a lack of local thermal equilibrium.

According to the numerical results obtained in the analysis of the validity of local thermal equilibrium in the one-dimensional model, the empty spaces between the outermost segments in the kinetic temperature profiles shown in the trapped ion systems, as well as the variations leading to the small oscillations in the intermediate axial region, see Figs. 6 and 8, would correspond to regions of lack of local thermal equilibrium. These regions, where the probability of presence of ions becomes very small, in this three-dimensional system would be associated with local maxima of the global potential energy surface defined by the trap and the Coulomb repulsion. We stress that this interesting issue requires further consideration in future work. In this manner, the role of dimensionality and of more complex dynamics in three-dimensional systems can be further analyzed in relation to the local thermal equilibrium assumption and transport properties, as suggested in Ref. [57].

## V. CONCLUSIONS

We have considered two-species trapped ion systems exposed to a temperature gradient and analyzed their behavior in the nonequilibrium steady state. We have assumed spatially distributed thermal reservoirs that are emulated by different laser beams located at both ends of the axial axis of the trap and tuned to act only on one of the two ion species. To study the dynamics we have considered a three-dimensional model which fully takes into account the many-body Coulomb interaction among the ions and numerically simulated the classical Langevin equations.

We have illustrated the spatial segregation of the two simultaneously confined ion species due to the mass dependence of the secular frequencies of the trap. The analysis of the spatial probability densities in the steady state has shown that the presence of the heavier ion species in the bicrystals enhances the ion delocalization, in comparison with the one observed in the lighter ion monocrystal with the same number of components and under identical trapping conditions. The lighter ions in the bicrystal remain strongly confined around equilibrium positions arranged along the axial trap axis, whereas the weaker confinement acting on the heavier ions allows them to undergo structural phase transitions and adopt two-dimensional and three-dimensional configurations

in which they can exhibit a high delocalization. In symmetrical traps with the same transverse frequencies these heavier ions are delocalized in a series of rings arranged perpendicular to the axial axis, similarly to those corresponding to the helical configuration in monocrystals. In the case of asymmetrical traps with unequal transverse frequencies the heavier ions are delocalized in planar configurations arranged on both sides of the axial axis and contained in the plane perpendicular to the direction with the highest frequency, similarly to the zigzag configuration characteristic of monocrystals.

We have analyzed the steady-state kinetic temperature profiles for bicrystals exposed to trapping conditions leading ion conformations of different dimensionality. Under sufficiently strong confinement conditions in which the ions of the two species are confined along the axial axis of the trap the temperature exhibits the characteristic flat profile of harmonic systems. The delocalization that arises as a consequence of the relaxation of the trapping conditions and/or the presence of heavier ions leads to the appearance of temperature profiles with nonzero gradients. As in monocrystals, such gradient remains uniform in symmetric traps, whereas in asymmetric traps the temperature profiles bend and are not fully linear in the bulk.

The analysis of the central gradient of the temperature profile has shown that its magnitude increases as the range of delocalization of the ions across the trap becomes more extensive. We have shown that a higher ion delocalization approaches the magnitude of the temperature gradient in the bulk to the value expected in a Fourier-type behavior. The gradient closest to this limit value has been obtained for the bicrystal containing the heaviest ion species confined in the symmetrical trap of weaker transverse confinement.

We have also shown the correlation between the behavior of the kinetic temperature on small scales and the spatial delocalization of the ions through the structure of the trapping potential energy surface. This has been made explicit by analyzing a simple model of a Brownian particle confined within a known potential energy surface in nonequilibrium due to interaction with two different thermal baths.

Our results indicate a possible limitation in the design of an experimental setup to study heat transport in a trapped ion system. Specifically, the parameters of the trap and the masses of the ion species should be such that the confinement is strong enough to maintain ions of species A confined at the ends where the thermal reservoirs are located. As it has been shown, an excessive increase in the ion delocalization can cause a displacement of the ions of species B toward the ends and an accumulation of the ions of species A to the internal region where they do not interact with the baths. Thus, the necessary conditions for an energy transport through the system would not be met. Our analysis indicates that to avoid this effect, symmetric traps in which the two transverse confinement frequencies of each ion species are equal would be more convenient to perform heat transport experiments than traps with unequal transverse confinement.

#### ACKNOWLEDGMENTS

We thank J. P. Palao for fruitful discussions. This project was funded by the Spanish MICINN and European Union (FEDER) (Grant No. FIS2017-82855-P). We thank the GOTA Research Group of La Laguna University and A. Muñoz for access to their computer facilities.

- 
- [1] T. Pruttivarasin, M. Ramm, I. Talukdar, A. Kreuter, and H. Häffner, Trapped ions in optical lattices for probing oscillator chain models, *New J. Phys.* **13**, 075012 (2011).
  - [2] M. Ramm, T. Pruttivarasin, and H. Häffner, Energy transport in trapped ion chains, *New J. Phys.* **16**, 063062 (2014).
  - [3] G. D. Lin and L. M. Duan, Equilibration and temperature distributions in a driven ion chain, *New J. Phys.* **13**, 075015 (2011).
  - [4] A. Bermudez, M. Bruderer, and M. B. Plenio, Controlling and Measuring Quantum Transport of Heat in Trapped-Ion Crystals, *Phys. Rev. Lett.* **111**, 040601 (2013).
  - [5] A. Ruiz, D. Alonso, M. B. Plenio, and A. del Campo, Tuning heat transport in trapped-ion chains across a structural phase transition, *Phys. Rev. B* **89**, 214305 (2014).
  - [6] N. Freitas, E. Martinez, and J. P. Paz, Heat transport through ion crystals, *Phys. Scr.* **91**, 013007 (2015).
  - [7] C. Cormick and C. Schmiegelow, Noise-induced transport in the motion of trapped ions, *Phys. Rev. A* **94**, 053406 (2016).
  - [8] A. Bermudez and T. Schaetz, Quantum transport of energy in controlled synthetic quantum magnets, *New J. Phys.* **18**, 083006 (2016).
  - [9] F. Cosco, M. Borrelli, P. Silvi, S. Maniscalco, and G. De Chiara, Nonequilibrium quantum thermodynamics in Coulomb crystals, *Phys. Rev. A* **95**, 063615 (2017).
  - [10] A. Ruiz-García, J. J. Fernández, and D. Alonso, Delocalization and heat transport in multidimensional trapped ion systems, *Phys. Rev. E* **99**, 062105 (2019).
  - [11] M. A. Simón, S. Martínez-Garaot, M. Pons, and J. G. Muga, Asymmetric heat transport in ion crystals, *Phys. Rev. E* **100**, 032109 (2019).
  - [12] S. Lepri, R. Livi, and A. Politi, Thermal conduction in classical low-dimensional lattices, *Phys. Rep.* **377**, 1 (2003).
  - [13] A. Dhar, Heat transport in low-dimensional systems, *Adv. Phys.* **57**, 457 (2008).
  - [14] Y. Dubi and M. Di Ventra, *Colloquium*: Heat flow and thermoelectricity in atomic and molecular junctions, *Rev. Mod. Phys.* **83**, 131 (2011).
  - [15] C. Sevik, H. Sevincli, G. Cuniberti, and T. Cagin, Phonon engineering in carbon nanotubes by controlling defect concentration, *Nano Lett.* **11**, 4971 (2011).
  - [16] V. Lee, C. H. Wu, Z. X. Lou, W. L. Lee, and C. W. Chang, Divergent and Ultrahigh Thermal Conductivity in Millimeter-Long Nanotubes, *Phys. Rev. Lett.* **118**, 135901 (2017).

- [17] P. Kim, L. Shi, A. Majumdar, and P. L. McEuen, Thermal Transport Measurements of Individual Multiwalled Nanotubes, *Phys. Rev. Lett.* **87**, 215502 (2001).
- [18] M. Fujii, X. Zhang, H. Xie, H. Ago, K. Takahashi, T. Ikuta, H. Abe, and T. Shimizu, Measuring the Thermal Conductivity of a Single Carbon Nanotube, *Phys. Rev. Lett.* **95**, 065502 (2005).
- [19] A. A. Balandin, Thermal properties of graphene and nanostructured carbon materials, *Nat. Mater.* **10**, 569 (2011).
- [20] E. Pop, D. Mann, Q. Wang, K. Goodson, and H. Dai, Thermal conductance of an individual single-wall carbon nanotube above room temperature, *Nano Lett.* **6**, 96 (2006).
- [21] G. Birkel, S. Kassner, and H. Walther, Multiple-shell structures of laser-cooled  $^{24}\text{Mg}^+$  ions in a quadrupole storage ring, *Nature* **357**, 310 (1992).
- [22] I. Waki, S. Kassner, G. Birkel, and H. Walther, Observation of Ordered Structures of Laser-Cooled Ions in a Quadrupole Storage Ring, *Phys. Rev. Lett.* **68**, 2007 (1992).
- [23] D. H. E. Dubin and T. M. O'Neil, Trapped noneutral plasmas, liquids, and crystals (the thermal equilibrium states), *Rev. Mod. Phys.* **71**, 87 (1999).
- [24] S. Mavadia, J. F. Goodwin, G. Stutter, S. Bharadia, D. R. Crick, D. M. Segal, and R. C. Thompson, Control of the conformations of ion Coulomb crystals in a Penning trap, *Nat. Commun.* **4**, 2571 (2013).
- [25] L. L. Yan, W. Wan, L. Chen, F. Zhou, S. J. Gong, X. Tong, and M. Feng, Exploring structural phase transitions of ion crystals, *Sci. Rep.* **6**, 21547 (2016).
- [26] H. Häffner, C. F. Roos, and R. Blatt, Quantum computing with trapped ions, *Phys. Rep.* **469**, 155 (2008).
- [27] Ch. Schneider, D. Porras, and T. Schaetz, Experimental quantum simulations of many-body physics with trapped ions, *Rep. Prog. Phys.* **75**, 024401 (2012).
- [28] R. Blatt and C. F. Roos, Quantum simulations with trapped ions, *Nat. Phys.* **8**, 277 (2012).
- [29] P. K. Ghosh, *Ion Traps* (Clarendon Press, London, 1995).
- [30] J. P. Schiffer, Phase Transitions in Anisotropically Confined Ionic Crystals, *Phys. Rev. Lett.* **70**, 818 (1993).
- [31] G. Piacente, I. V. Schweigert, J. J. Betouras, and F. M. Peeters, Generic properties of a quasi-one-dimensional classical Wigner crystal, *Phys. Rev. B* **69**, 045324 (2004).
- [32] S. Fishman, G. De Chiara, T. Calarco, and G. Morigi, Structural phase transitions in low-dimensional ion crystals, *Phys. Rev. B* **77**, 064111 (2008).
- [33] R. W. Hasse and J. P. Schiffer, The structure of the cylindrically confined Coulomb lattice, *Ann. Phys. (NY)* **203**, 419 (1990).
- [34] R. Nigmatullin, A. del Campo, G. De Chiara, G. Morigi, M. B. Plenio, and A. Retzker, Formation of helical ion chains, *Phys. Rev. B* **93**, 014106 (2016).
- [35] L. Hornekær, *Single- and Multi-Species Coulomb Ion Crystals: Structures, Dynamics and Sympathetic Cooling*, Ph.D. thesis, University of Aarhus, Denmark (2000).
- [36] L. Hornekær, N. Kjærgaard, A. M. Thommesen, and M. Drewsen, Structural Properties of Two-Component Coulomb Crystals in Linear Paul Traps, *Phys. Rev. Lett.* **86**, 1994 (2001).
- [37] C. B. Zhang, D. Offenber, B. Roth, M. A. Wilson, and S. Schiller, Molecular-dynamics simulations of cold single-species and multispecies ion ensembles in a linear Paul trap, *Phys. Rev. A* **76**, 012719 (2007).
- [38] B. Roth, P. Blythe, and S. Schiller, Motional resonance coupling in cold multispecies Coulomb crystals, *Phys. Rev. A* **75**, 023402 (2007).
- [39] G. Morigi and H. Walther, Two-species Coulomb chains for quantum information, *Eur. Phys. J. D* **13**, 261 (2001).
- [40] T. Fogarty, E. Kajari, B. G. Taketani, A. Wolf, Th. Busch, and G. Morigi, Entangling two defects via a surrounding crystal, *Phys. Rev. A* **87**, 050304(R) (2013).
- [41] R. C. Thompson, Ion Coulomb crystals, *Contemp. Phys.* **56**, 63 (2015).
- [42] T. Matthey, J. P. Hansen, and M. Drewsen, Coulomb Bicrystals of Species with Identical Charge-to-Mass Ratios, *Phys. Rev. Lett.* **91**, 165001 (2003).
- [43] M. Drewsen, I. Jensen, J. Lindballe, N. Nissen, R. Martinussen, A. Mortensen, P. Staunum, and D. Voigt, Ion Coulomb crystals: A tool for studying ion processes, *Inter. J. Mass Spect.* **229**, 83 (2003).
- [44] S. Schmidt, T. Murböck, Z. Andelkovic, G. Birkel, K. König, W. Nörthershäuser, R. C. Thompson, and M. Vogel, Sympathetic cooling in two-species ion crystals in a Penning trap, *J. Mod. Opt.* **65**, 538 (2018).
- [45] H. G. Dehmelt, Radiofrequency spectroscopy of stored ions I: Storage, *Adv. Atom. Mol. Phys.* **3**, 53 (1968).
- [46] H. G. Dehmelt, Radiofrequency spectroscopy of stored ions II: Spectroscopy, *Adv. Atom. Mol. Phys.* **5**, 109 (1969).
- [47] F. Diedrich and H. Walther, Nonclassical Radiation of a Single Stored Ion, *Phys. Rev. Lett.* **58**, 203 (1987).
- [48] R. Blümel, J. M. Chen, E. Peik, W. Quint, W. Schleich, Y. R. Shen, and H. Walther, Phase transitions of stored laser-cooled ions, *Nature* **334**, 309 (1988).
- [49] D. J. Wineland and W. M. Itano, High-resolution spectroscopy of stored ions, *Adv. Atom. Mol. Phys.* **19**, 135 (1983).
- [50] D. Leibfried, R. Blatt, C. Monroe, and D. Wineland, Quantum dynamics of single trapped ions, *Rev. Mod. Phys.* **75**, 281 (2003).
- [51] See, for example, W. D. Phillips, Laser cooling and trapping of neutral atoms, in *Laser Manipulation of Atoms and Ions*, edited by E. Arimondo, W. D. Phillips, and F. Strumia, *Proceedings of the International School of Physics "Enrico Fermi," Course CXVIII* (North-Holland, Amsterdam, 1992), p. 289.
- [52] K. Momma and F. Izumi, VESTA 3 for three-dimensional visualization of crystal, volumetric and morphology data, *J. Appl. Crystallogr.* **44**, 1272 (2011).
- [53] D. Alonso, A. Ruiz, and I. de Vega, Polygonal billiards and transport: Diffusion and heat conduction, *Phys. Rev. E* **66**, 066131 (2002).
- [54] D. Alonso, A. Ruiz, and I. de Vega, Transport in polygonal billiards, *Physica D (Amsterdam)* **187**, 184 (2004).
- [55] T. Mai, A. Dhar, and O. Narayan, Equilibrium and Universal Heat Conduction in Fermi-Pasta-Ulam Chains, *Phys. Rev. Lett.* **98**, 184301 (2007).
- [56] V. Kannan, A. Dhar, and J. L. Lebowitz, Nonequilibrium stationary state of a harmonic crystal with alternating masses, *Phys. Rev. E* **85**, 041118 (2012).
- [57] L. Wang, S. Liu, and B. Li, Validity of local thermal equilibrium in anomalous heat diffusion, *New J. Phys.* **21**, 083019 (2019).